Hindawi
Wireless Communications and Mobile Computing
Volume 2018, Article ID 6369517, 12 pages
https://doi.org/10.1155/2018/6369517

Research Article

Indoor Corridor Wideband Radio Propagation Measurements and Channel Models for 5G Millimeter Wave Wireless Communications at 19 GHz, 28 GHz, and 38 GHz Bands

Ahmed M. Al-samman, Tharek Abd Rahman, and Marwan Hadri Azmi

Department Wireless Communication Centre, Faculty of Electrical Engineering, Universiti Teknologi Malaysia, 81310 Johor, Malaysia

Correspondence should be addressed to Ahmed M. Al-samman; ahmedsecure99@gmail.com
and Tharek Abd Rahman; tharek@fke.utm.my

Received 16 September 2017; Revised 16 January 2018; Accepted 23 January 2018; Published 8 March 2018

Academic Editor: Dajana Cassioli

This paper presents millimeter wave (mmWave) measurements in an indoor environment. The high demands for the future applications in the 5G system require more capacity. In the microwave band below 6 GHz, most of the available bands are occupied; hence, the microwave band above 6 GHz and mmWave band can be used for the 5G system to cover the bandwidth required for all 5G applications. In this paper, the propagation characteristics at three different bands above 6 GHz (19, 28, and 38 GHz) are investigated in an indoor corridor environment for line of sight (LOS) and non-LOS (NLOS) scenarios. Five different path loss models are studied for this environment, namely, close-in (CI) free space path loss, floating-intercept (FI), frequency attenuation (FA) path loss, alpha-beta-gamma (ABG), and close-in free space reference distance with frequency weighting (CIF) models. Important statistical properties, such as power delay profile (PDP), root mean square (RMS) delay spread, and azimuth angle spread, are obtained and compared for different bands. The results for the path loss model found that the path loss exponent (PLE) and line slope values for all models are less than the free space path loss exponent of 2. The RMS delay spread for all bands is low for the LOS scenario, and only the directed path is contributed in some spatial locations. For the NLOS scenario, the angle of arrival (AOA) is extensively investigated, and the results indicated that the channel propagation for 5G using high directional antenna should be used in the beamforming technique to receive the signal and collect all multipath components from different angles in a particular mobile location.

1. Introduction

The ever-growing data rate demand as well as the shortage of current frequency resources are the main challenges for the upcoming fifth generation (5G) of mobile communications [1–4]. The congestion of the current frequency band (below 6 GHz) and the narrowness of the wireless bandwidth are key problems for fifth generation wireless networks. Exploitation of the unused microwave and millimeter wave (mmWave) spectrum (spectrum between 6 and 300 GHz) is an efficient solution to overcome the 5G network's enormous data demand. With the huge bandwidth available in the millimeter wave band, mmWave communications have been proposed as an important part of the 5G mobile network that can provide multi-gigabit communication services such as ultrahigh definition video (UHDV) and high definition television (HDTV) [5]. As with any wireless communication, the study of signal propagation is important for designing and modeling mmWave systems. Thus, characterization and modeling of such channel propagation in urban environments are some of the most important tasks in developing novel 5G mobile access networks. Recently, most research has focused on the 28 GHz band, the 38 GHz band, and the E-band (71–76 GHz and 81–86 GHz) [6]. In the past two decades, measurement campaigns were conducted in 28 GHz and 38 GHz mmWave bands for Local Multipoint Distribution Service (LMDS) [7, 8]. In addition, wideband NLOS measurements were performed by Violette et al. at the 9.6, 28.8, and 57.6 GHz bands in downtown Denver, where the results showed significant signal attenuation due

to obstruction by large buildings [9]. Propagation through a canopy of orchard trees was measured using continuous wave (CW) signals at 9.6, 28.8, and 57.6 GHz [10].

Several channel measurements have been conducted at some mmWave bands such as 6, 10, 11, 15, 18, 19, 26, 28, 32, and 38 GHz bands. In [11], the propagation characteristics of mmWaves were investigated in an indoor corridor environment for the line of sight (LOS) scenario at 6.5, 10.5, 15, 19, 28, and 38 GHz bands. In [12], frequency domain measurements were conducted at 28 GHz in a laboratory using a vector network analyzer (VNA) with 1 GHz bandwidth and 1 ns time resolution to estimate the channel parameters for multipath components (MPCs). The path loss, shadowing, polarization properties, and root mean square (RMS) delay spread were obtained. Some measurements have been conducted by New York University (NYU) in the 28 GHz and 73 GHz frequency bands in a typical indoor office environment [13–16]. Three large-scale propagation path loss models for use over the entire microwave and mmWave radio spectrum, namely, the alpha-beta-gamma (ABG) model, the close-in (CI) free space reference distance model, and the CI model with a frequency-weighted path loss exponent (CIF), were studied and compared for the bands from 2 to 73 GHz with different frequency bands [13]. Moreover, indoor measurements for wireless and backhaul communications have been conducted in the frequency band of 72 GHz [17, 18]. At Finland's Aalto University, mmWave measurements have been conducted in the 60 GHz and 70 GHz frequency bands [19, 20]. Measurement in mmWave has also attracted research interest by corporations, for example, Samsung, Ericsson, Qualcomm, and Huawei [21, 22]. Hur et al. have conducted measurements in the 28 GHz band in the indoor environment [23]. Moreover, different academic researchers have conducted other measurements for several types of indoor environments at the 28 GHz band [12, 24]. Wang et al. [25] have conducted wideband channel measurement at 26 GHz in an open office LOS environment.

In all of the previously conducted mmWave measurements related to the 5G vision, the candidate frequencies for 5G wireless communications were still under research. In addition, investigation of the time and angle dispersion spread parameters was limited in most previous 5G mmWave measurements. The focus of ongoing research related to mmWave communications is the study of propagation characteristics, channel modeling, beamforming, and medium access control design. Extensive research is still required to enable deployment of mmWave communications in cellular systems.

In this paper, characterization of an extensive indoor propagation channel is performed for three different mmWave bands above 6 GHz. The channel characteristics are investigated based on five path loss models. The power, time, and angle dispersion are analyzed for line of sight (LOS) and non-LOS (NLOS) scenarios. These parameters are studied based on the root mean square delay and angle spread, excess delay, and angle of arrival (AOA).

The rest of the paper is organized as follows. The measurement equipment and environment are described in Section 2. Section 3 discusses the channel model and postprocessing. The path loss, time, and angular dispersion parameters are described in Section 4. The path loss model results and analysis are presented in Section 5. Section 6 provides an analysis of the power, time, and angle dispersion parameters. Finally, the conclusion is drawn in Section 7.

2. Measurement Setup

For sounding signal acquisition, the measurement setup for this work is described in detail as follows. The transmitter side of the wideband channel sounder consisted of an arbitrary waveform generator (AWG) M8190A, up-converter E8267D, and rubidium clock 6689. The M8190A AWG was used to generate wideband differential baseband in-phase quadrature (IQ); it could also output direct intermediate frequency (IF) signals with channel sounding. The baseband arbitrary waveform signal provided 1-ns multipath resolution from a pseudorandom binary sequence (PRBS). The E8267D up-converter could up-convert this differential baseband IQ into a radio frequency (RF) carrier (up to 40 GHz) with wide modulation bandwidth and could adjust the output power with its Automatic Line Controller (ALC) circuit. Two 6689 Pendulum clock units (one for Tx and one for Rx) were used in the channel sounder system for synchronization between transmitter and receiver; they could provide a high precision 10 MHz reference signal to all of the instruments with $\leq 1e-11$ accuracy and $\leq 3e-11$ stability. The trigger signals could be derived from a rubidium clock or 33522B Function Generation system. At the receiver side of the wideband channel sounder, a down-converter M9362AD01 was used to down-convert RF frequencies (up to 40 GHz) to IF, a hybrid amplifier/attenuator M9352A was used to amplify the IF signal, and finally, a 12-bit high speed digitizer M9703A of 1 GHz bandwidth (interleaving mode) was used to acquire the IF signal. An N5173B was used as the local oscillator (LO) for the down-converter M9362AD01. An M9300A was the Frequency Reference module that took in an external 10 MHz and output 10 MHz and 100 MHz standard references; all of the equipment could keep the relative phase stable (phase locked). Similar to a Tx 6689, an Rx 6689 Pendulum clock unit also provided a standard 10 MHz reference for all of the instruments. The Rx trigger signal was loaded by a function generator 33522B. The arbitrary waveform channel sounding (AWCS) signal and frequency settings of the Tx and Rx are provided in Table 1. Using this setup with a 1-ns multipath resolution, an extensive set of mmWave propagation measurements was conducted at 19, 28, and 38 GHz center frequencies. Figure 1 shows the photograph of the Tx and Rx apparatuses.

The measurements were conducted along a corridor on the second floor of the Menara Tun Razak Building in the Universiti Teknologi Malaysia (UTM) campus, Kuala Lumpur, Malaysia. The Menara Tun Razak Building is a 17-story building with discussion rooms and faculty offices. The size of the corridor is 1.80 m × 67 m and the ceiling height is 3 m. The corridor has plywood and glass doors, and the walls are constructed from concrete, glass, and gypsum board. The floor ground is covered with glazed ceramic tiles, and the corridor ceiling is composed of fiberglass

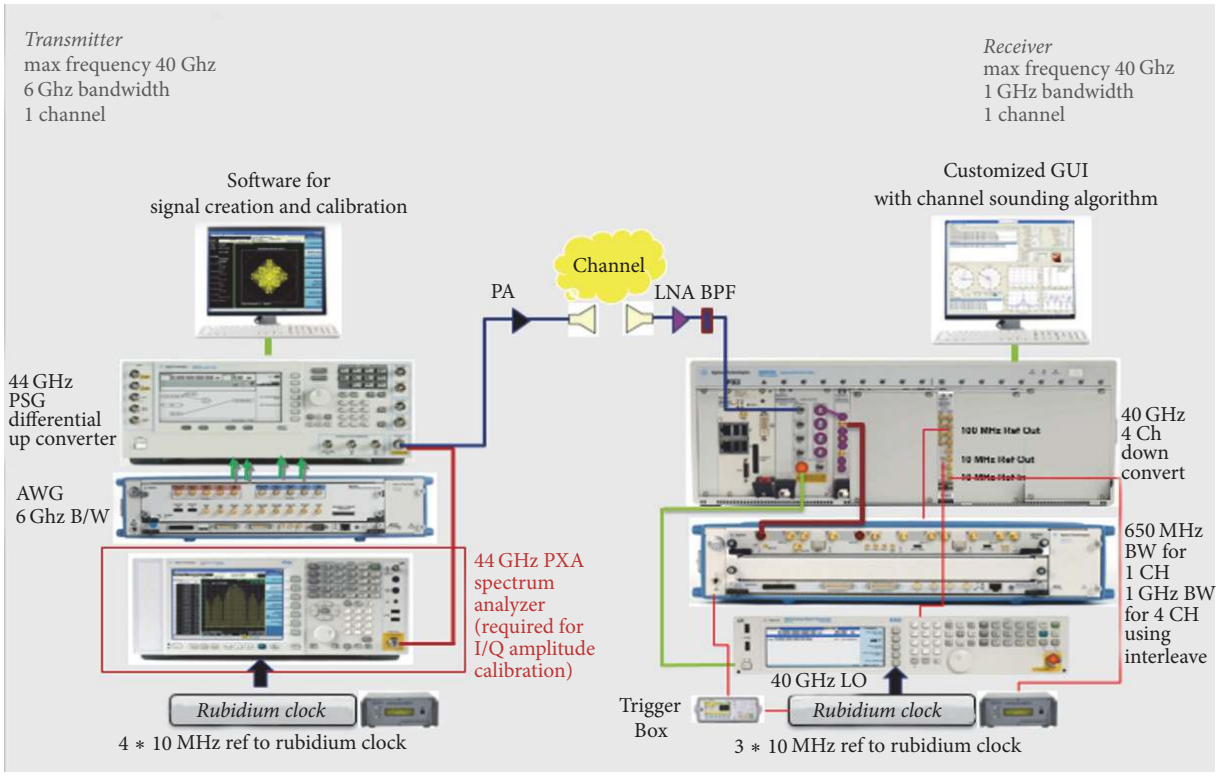

Figure 1: Photograph of the Tx and Rx apparatuses for the 5G channel sounder.

Table 1: Measurement setup parameters.

Carrier frequency (GHz)	19	28	38
AWCS signal		10th order PRBS (length = 1024)	
AWCS chip rate (Mcps)		1000	
AWCS chip duration (ns)		1	
Digitizer sampling rate (Gsps)		3.2	
PDP update rate (PDPs/second)		100	
RF BW (GHz)		1	
Rx LO power (dBm)		10	
Rx sensitivity		−120 dBm	
Tx power (dBm)		0	
Tx and Rx antenna gain (dBi)	11.6	11.6	15.2
HPBW (degrees)	46.4	44.8	28.3
Tx antenna height (m)		1.7	
Rx antenna height (m)		1.5	
Tx, Rx polarization		Vertical	

materials. Figure 2 shows the floor plan and description of the measurement environment. During the measurements, the Tx part is stationary and the Rx part is moved along a corridor, as depicted in Figure 2. The Tx antenna was placed 1.7 m above the floor to emulate an indoor hotspot in the wall, and the Rx antenna was placed 1.5 m above the floor (typical handset level heights). The measurement was started with the Rx antenna located 1 m away from transmitter, and the received signal is recorded while keeping the Rx stationary at that position. Next, the Rx was moved 1 m farther away from its starting location, and the stationary measurements were repeated. The process was repeated likewise at 63 different locations of the Rx for the LOS scenario, each 1 m away from the previous adjacent location.

For the NLOS scenario, at the Tx-Rx separation distance of 18 m for the LOS scenario, the Rx antenna was moved by 3 m perpendicular to the LOS path, where the wall blocks the Tx from the Rx, and then the Rx was moved by 1 m up to 6 m, as shown in Figure 2. The Rx antenna was rotated by different angles at each NLOS location for all measured frequencies. With the zero degree (0°) rotation referring to the alignment of the Rx antenna with the Tx path, the Rx antenna was rotated, as shown in Figure 2. Based on these measurements, an extensive indoor channel characterization for mmWave bands is investigated as shown in Figure 2.

3. Data Processing and Channel Model

First, the influence of the measurement system was excluded from the recorded channel datasets using the system calibration procedure described in [26]. Next, the data were subjected to postprocessing using SystemVue software [27] and MATLAB Toolbox. The CIR was extracted by cross correlation between the received waveform and the transmitted arbitrary waveform signal. The Space-Alternating Generalized Expectation-maximization (SAGE) algorithm [28–30]

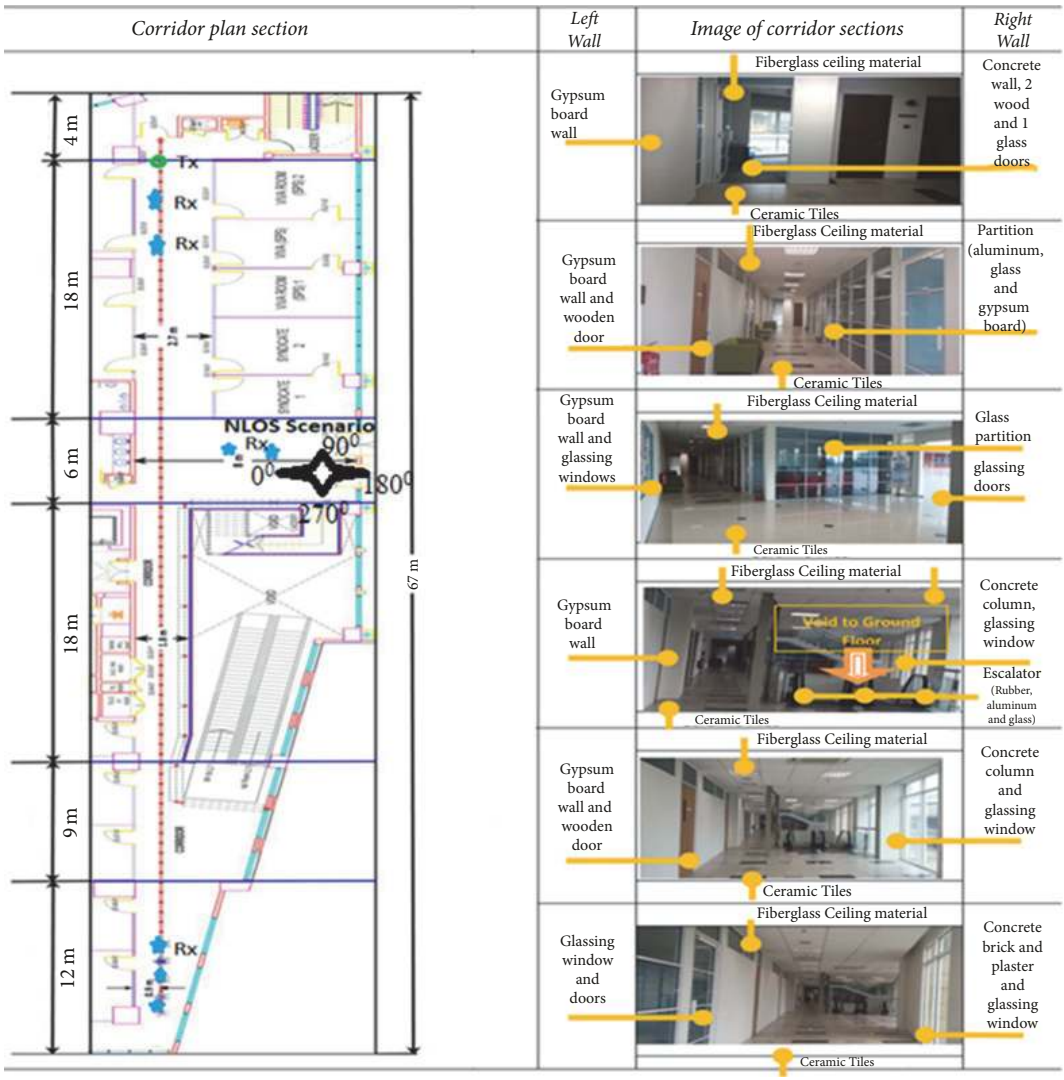

Figure 2: Floor plan and description of the environment.

was used to extract the parameters of MPCs, including path delay and path gain. The SAGE algorithm allowed an iterative determination of the maximum-likelihood estimation. The SAGE algorithm resolved the MPCs by an interference-cancellation, where the MPCs already estimated were subtracted from the considered signal.

The channel is excited by a transmitted pulse leading the receiver part to generate a summation of modified pulses with different attenuation factors and different time delays that represent the received waveform. The received waveform is called a multipath profile. The individual pulses arrived at the receiver through different paths, which are referred to as MPCs. The real CIR can be represented as a superposition of these paths, as in (1), that is, assuming no dispersion within the individual pulse [31].

$$h(\tau) = \sum_{i=1}^{L} a_i \delta(\tau - m_i), \tag{1}$$

where a_i and m_i are the ith path gain and delay, respectively.

For time-varying channels, (1) can be modified as [31]

$$h(t,\tau) = \sum_{i=1}^{L} a_i(t)\,\delta(\tau - m_i(t)), \tag{2}$$

where t is either the time or the spatial location. Assuming that the transmitter moves at a constant velocity away from the receiver, we can convert between the time and spatial location.

Denoting by $q(\tau)$ the pulse transmissions waveform sent by the transmitter, the delayed received waveforms $r(\tau)$ after propagating through the channel of (1) become

$$r(\tau) = q(\tau) \otimes h(\tau) = \sum_{i} \alpha_i q(\tau - m_i). \tag{3}$$

Based on the above equation, the power delay profile (PDP) can be expressed as

$$P(\tau) = \sum_{i} {\alpha_i}^2 q^2(\tau - m_i). \tag{4}$$

The path loss and time and angular dispersion parameters are derived from (4) as follows.

4. Path Loss, Time, and Angular Dispersion Parameters

The path loss represents the fundamental quantities characterizing the wireless propagation channel and influencing the performance of any communication system. It is the inverse of the path gain, which is the amount of the signal power received. In a narrowband system, the path loss is defined as the amount of decay in the received power at a certain (carrier) frequency. For wideband and UWB radio, the path loss can be derived from the power of MPCs, which includes the joint effects of attenuation and time dispersion. The received signal energy can be calculated from the measured multipath profile as [32, 33]

$$P = \sum_i {\alpha_i}^2. \tag{5}$$

Denoting the average of the received signal energy at distance d using $\overline{P}(d)$ and at reference distance d_0 using $\overline{P}(d_0)$, the logarithmic value of the path loss can be computed using

$$\mathrm{PL}\,(d) = -10\log_{10}\left[\frac{\overline{P}\,(d)}{\overline{P}\,(d_0)}\right]. \tag{6}$$

The time dispersion and angular dispersion play a key role in modern cellular systems [34]. The PDP of the received signal provides a good indication of the dispersion of the transmitted power over various paths. The time dispersion characteristics show the distribution of the power relative to the first arriving MPC. The time dispersion characteristics are usually quantified in terms of the mean excess delay and the RMS delay spread. To obtain these parameters, the PDP is normalized and all signals below a specific threshold x dB relative to the maximum are considered zero for the analysis [5, 35]. The required time for the energy of the received waveform to fall x dB relative to the maximum is defined as the maximum excess delay of the PDP. The RMS delay spread is computed as [36]

$$\tau_{\mathrm{rms}} = \sqrt{\frac{\sum_i p_i \cdot \left(m_i - m_1 - \tau_m\right)^2}{\sum_i p_i}}, \tag{7}$$

where τ_{rms} is the RMS delay spread that is defined by the square root of the second central moment of a power delay profile, p_i is the power for the ith path, m_i is the arrival time of the ith MPC, m_1 is the first path arrival time, and τ_m is the mean excess delay that can be represented by the first moment of the PDP as

$$\tau_m = \frac{\sum_i p_i \cdot \left(m_i - m_1\right)}{\sum_i p_i}. \tag{8}$$

In addition to the time dispersion, wireless propagation channels also show angular dispersion and determine the interaction between antennas and channels. In the wireless channel model, the RMS angular spread of arrival (ASA) plays an important role and is calculated as follow [37]:

$$\Lambda_{\mathrm{ASA}} = \sqrt{\frac{\sum_l p_l \cdot \left(\varphi_l - \mu_{\mathrm{ASA}}\right)^2}{\sum_l p_l}}, \tag{9}$$

where p_l is the power for lth path, φ_l is the angle of arrival (AOA), and μ_{ASA} is the mean of the angle and is defined as

$$\mu_{\mathrm{ASA}} = \frac{\sum_l p_l \cdot \varphi_l}{\sum_l p_l}. \tag{10}$$

5. Path Loss Models, Results, and Analysis

In this paper, different path loss models are used to investigate the path loss in three different candidate bands for the 5G system. The close-in (CI) free space path loss model is a physically based model that uses the free space path loss (FSPL) at 1 m as the reference point (anchor-point) to estimate the path loss at different distances and spatial locations. In this work, we used the measured path loss at the anchor-point as the reference. The CI model can be calculated as [38]

$${P_L}^{\mathrm{CI}}\,(f, d)\,[\mathrm{dB}] = P_L\,(f, d_0) + 10n\log_{10}\left(\frac{d}{d_0}\right) + X_\sigma, \tag{11}$$

where $P_L(f, d)$ is the path loss at different frequencies with various Tx-Rx separation distance, n is the path loss exponent (PLE), $P_L(f, d_0)$ is the path loss in dB at a close-in (CI) distance, d_0, of 1 m, and X_σ is a zero-mean Gaussian-distributed random variable with standard deviation σ dB (shadowing effect) [39].

Figure 3 shows the scatter plots of the path loss and the best fit CI model for the LOS scenario at 19, 28, and 38 GHz. It can be shown that the path loss increases as the separation distance and frequency are increased, where the highest path loss occurred at 38 GHz. The PLE values are 0.6, 0.6 and 1.3 for 19, 28, and 38 GHz, respectively. The PLE values for all frequencies are found to be less than those of the theoretical free space PLE ($n = 2$), indicating that the MPCs added up constructively from both side walls along the corridor (i.e., a wave-guiding effect). The signal degradation at the 38 GHz band of 13 dB/decade is twice the degradation of the signal at 19 and 28 GHz. The standard deviation values σ at the 19 and 38 GHz bands are identical (2.4 dB). At the 28 GHz band, the standard deviation value is 3.3 dB.

Another popular path loss model is the floating-intercept (FI) model, which is used in the WINNER II and 3GPP standards [13]. This model is not a physically based model; however, it is suitable for some bands and environments, where the floating-intercept (α) parameter is close to the FSPL at 1 m and the slope line (β) is comparable to the PLE. The FI model is defined as [11, 38]

$${P_L}^{\mathrm{FI}}\,(d)\,[\mathrm{dB}] = \alpha + 10\beta\log_{10}\,(d) + {X_\sigma}^{\mathrm{FI}}, \tag{12}$$

where ${X_\sigma}^{\mathrm{FI}}$ is the zero-mean Gaussian random variable dB with a standard deviation of σ dB.

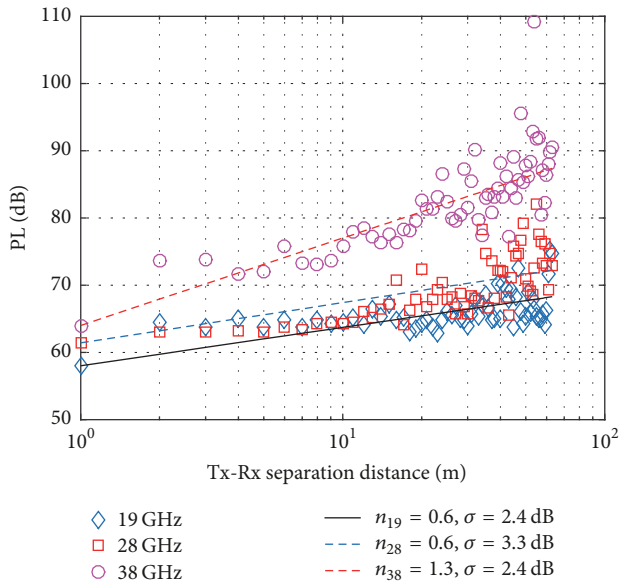

FIGURE 3: CI ($d0$ = 1 m) path loss model for the LOS scenario.

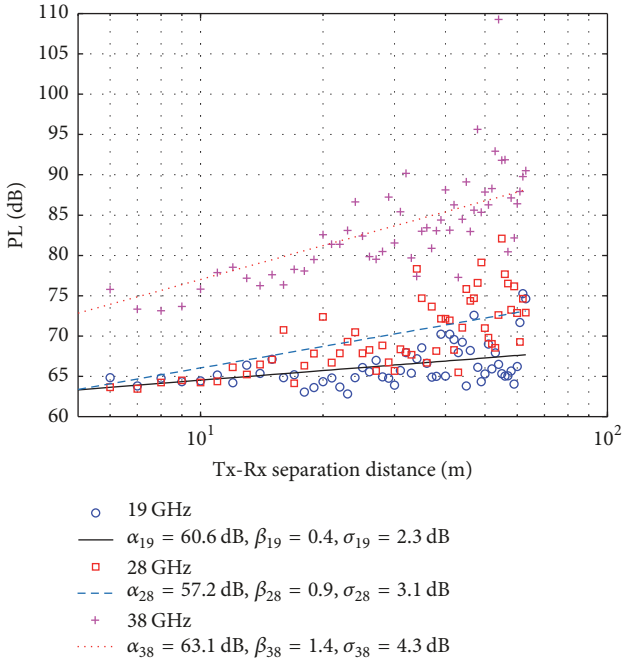

FIGURE 4: FI path loss model for the LOS scenario.

The FI path loss model at all measured bands is shown in Figure 4. The floating-intercept (α) values are 60.6 dB, 57.2 dB, and 63.1 dB for 19, 28, and 38 GHz, respectively. The α values deviate from FSPL at 1 m by 2.6 dB, 4.2 dB, and 0.9 dB for 19, 28, and 38 GHz, respectively. The slope line (β) values are 0.4, 0.9, and 1.4 for 19, 28, and 38 GHz, respectively. The β values are comparable with PLEs for the CI path loss model and the deviation of α values from FSPL at 1 m is reasonable for all bands. This implies that the FI path loss model, which is mostly used in the 3GPP for frequency bands below 6 GHz,

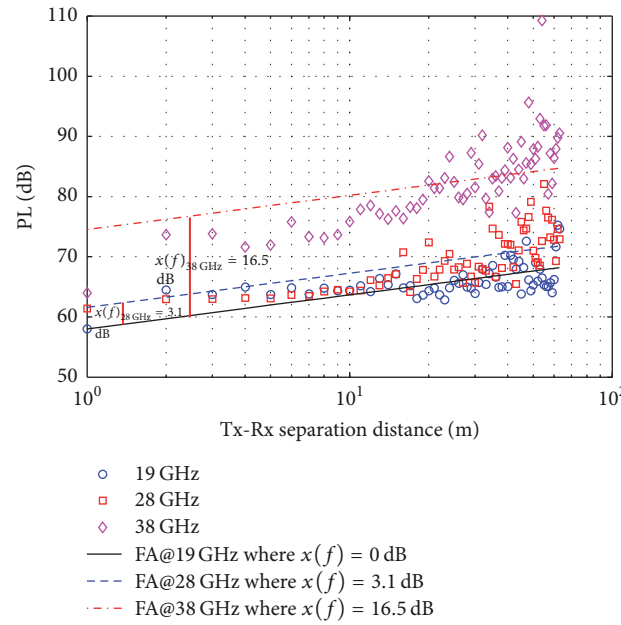

FIGURE 5: FA path loss model for the LOS scenario.

can be used with a suitable performance in mmWave bands for 5G systems. The standard deviation σ values for the FI model are 2.3 dB, 3.1 dB, and 4.3 dB for 19, 28, and 38 GHz, respectively.

To investigate the path loss with high frequency, the frequency attenuation (FA) path loss model is used, where the lowest measured frequency in a particular scenario is used as the reference frequency. The FA path loss model is defined as [11]

$$P_L^{\mathrm{FA}}(f,d)\,[\mathrm{dB}] = P_L(f_{\mathrm{ref}},d_0) + 10n_{\mathrm{ref}}\log_{10}\left(\frac{d}{d_0}\right) + XF(f) + X_\sigma^{\mathrm{FA}}, \tag{13}$$

where $P_L(f_{\mathrm{ref}},d_0)$ is the path loss in dB at the close-in distance d_0 of 1 m and the reference frequency f_{ref}. The f_{ref} in this model is defined as the lowest measured frequency using the same calibration environment; n_{ref} represents PLE at f_{ref}. The factor $XF(f)$ is the frequency attenuation factor in dB, which represents the signal drop with frequency, and X_σ^{FA} is the shadow fading term with a standard deviation of σ dB. The FA path loss model is a physical-based model and is simple, as the CI model. The reference frequency f_{ref} is 19 GHz and the PLE (n_{ref}) is 0.6.

The FA path loss model is shown in Figure 5. The $XF(f)$ attenuation values of the FA model are 3.1 dB and 16.5 dB for 28 and 38 GHz, respectively. Because 19 GHz is the reference frequency, the $XF(f)$ factor is 0 dB in this band. At the 28 GHz band, the signal degradation is low compared to the 19 GHz based on the $XF(f)$ attenuation factor. The standard deviation σ values for the FA model are 2.4 dB, 3.1 dB, and 4.5 dB for 19, 28, and 38 GHz, respectively.

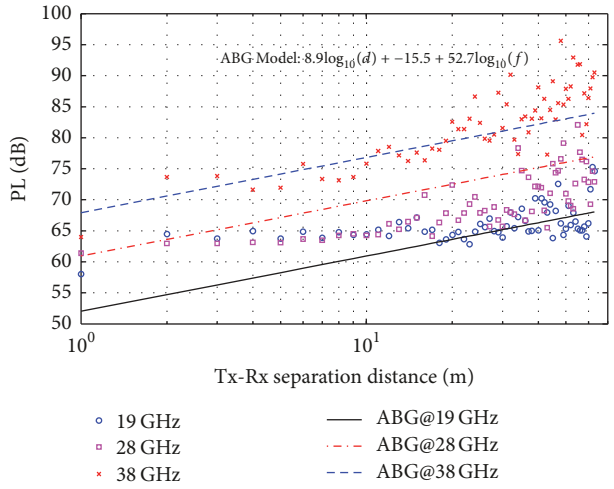

Figure 6: ABG multifrequency path loss model for the LOS scenario.

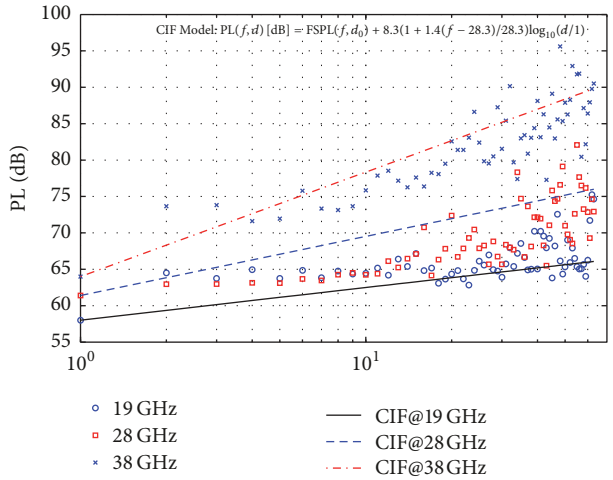

Figure 7: CIF multifrequency path loss model for the LOS scenario.

Because the path loss is measured at different bands, the multifrequency path loss models can be used to investigate the path loss for these bands. Here, the alpha-beta-gamma (ABG) and close-in free space reference distance with frequency weighting (CIF) path loss models are used for multifrequency path loss investigation. The ABG model includes a frequency dependent and distance-dependent term to describe path loss at various frequencies and is calculated as

$$P_L^{\mathrm{ABG}}(f,d)\,[\mathrm{dB}] = 10\alpha \log_{10}\left(\frac{d}{d_0}\right) + \beta + 10\gamma \log 10\left(\frac{f}{1\ \mathrm{GHz}}\right) + X_\sigma^{\mathrm{ABG}}, \quad d_0 = 1\ \mathrm{m}, \tag{14}$$

where α is the distance-dependent factor of path loss, γ is the frequency dependent factor, β is an optimized offset, and X_σ^{ABG} is the shadow fading term.

Figure 6 shows the ABG path loss model for all studied bands. The signal drop is found to be 8.9 dB/decade based on the distant-dependence factor ($\alpha = 0.89$). The optimized offset β and frequency dependent factor γ values are −15.5 dB and 5.27, respectively.

The CIF model is a frequency-weighted model that employs the same FSPL anchor at 1 m as that of the CI model and is defined as

$$P_L^{\mathrm{CIF}}(f,d)\,[\mathrm{dB}] = \mathrm{FSPL}(f,d_{\mathrm{ref}}) + 10n\left(1 + b\left(\frac{f-f_0}{f_0}\right)\right)\log_{10}(d) + \chi_\sigma^{\mathrm{CIF}}, \tag{15}$$

where n denotes the distance dependence of path loss and b is a linear frequency dependent factor of path loss over all considered frequencies. The parameter f_0 is the weighted frequency average of all measurements for each specific environment and scenario, found by summing, over all frequencies the number of measurements at a particular frequency and scenario, multiplied by the corresponding frequency, and dividing that sum by the entire number of measurements taken over all frequencies for that specific environment and scenario. Based on the particular environment and scenario and the number of measurements at a particular frequency in this work, $f_0 = 28.3$ GHz. The slope parameter is $n = 0.8$ with the linear frequency dependent factor $b = 1.4$ as depicted in Figure 7. It can be shown that with $n = 0.8$, the CIF path loss model can fit the measured data at all studied frequencies in this particular scenario.

6. Power, Delay, and Angle Dispersion Results and Analysis

The received power with different delay along the Tx-Rx separation distance in the 19 GHz band is shown in Figure 8. For all spatial locations along the corridor most of the received power arrived at the early excess delay (less than 10 ns). Furthermore, the maximum excess delay is less the 50 ns for all received paths with received power greater than −120 dBm (noise floor). The received power between −70 and −60 dBm appears in the directed path (LOS path) that represents the first path in the LOS scenario. This implies that when the high directional antenna is used, most power falls in the LOS path. For the MPCs with an excess delay of less than 5 ns, the received power is in the range of −80 to −70 dBm, which is degraded by 10 dBm compared to the range of directed paths, as shown in Figure 8. The MPCs have received power of −90 to −80 dBm with an excess delay of less than 10 ns. Few paths with power less than −100 dBm fall in the excess delay of more than 20 ns. It can be concluded that the power with a value greater than the noise floor by 10 dBm can be received at 19 GHz with 63 m Tx-Rx separation distance within a delay of less than 20 ns.

For the 28 GHz band, the power with different delays along the Tx-Rx separation distance is shown in Figure 9.

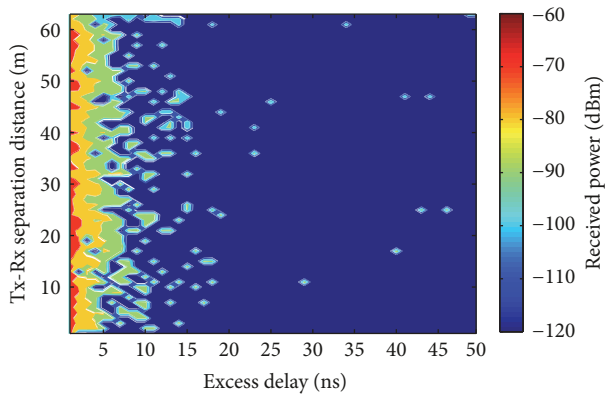

Figure 8: Received power at different delays for 19 GHz in all Tx-Rx separation distances considered for the LOS scenario.

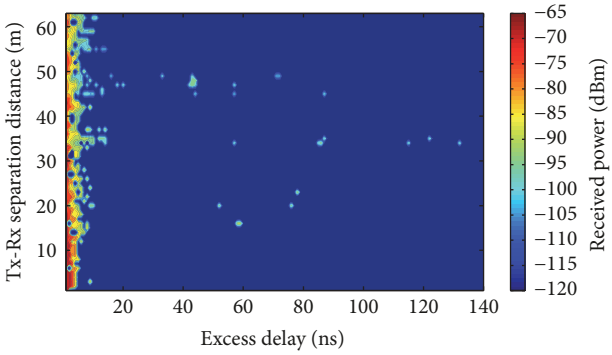

Figure 9: Received power at different delays for 28 GHz in all the considered Tx-Rx separation distances for the LOS scenario.

For this band, most of the received power is less than 10 ns; that is, most of the MPCs are received early. However, in some spatial locations, some MPC components are received at an excess delay greater than 100 ns and less than 140 ns, as shown in Figure 9. The received power with different delays along the Tx-Rx separation distance in the 38 GHz band is shown in Figure 10. In this band, only at the first 3 meters Tx-Rx separation distance is the received power greater than −75 dBm with almost no delay (LOS path only). For the Tx-Rx separation distance of less than 15 m, the received power varies between −85 and −80 dBm, with a delay of less than 4 ns. In this band, no MPCs have a delay greater than 15 ns.

The RMS delay spread versus Tx-Rx separation distance for LOS scenario is shown in Figure 11. The maximum delay spread is found to be less than 35 ns for all studied bands. Moreover, the delay spread is the lowest at the 38 GHz band, and the delay spread decreases as the frequency increases. This implies that, with increased directivity of the antenna (lower HPBW), most power is concentrated in the directed path and no more MPCs are contributed in the received signal. The maximum delay spread values are 32.3 ns, 25.3 ns, and 2.6 ns at the spatial locations of 47 m, 34 m, and 32 m for 19, 28, and 38 GHz, respectively. The mean delay spread values are 5.7 ns, 2.3 ns, and 1.1 ns for 19, 28, and 38 GHz, respectively. This implies that most MPCs fall in the early bins.

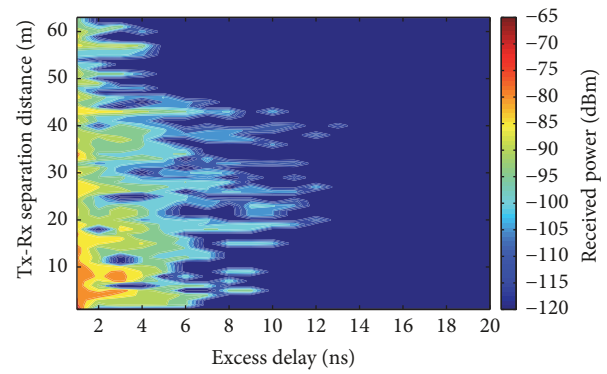

Figure 10: Received power at different delays for 38 GHz in all the considered Tx-Rx separation distances for the LOS scenario.

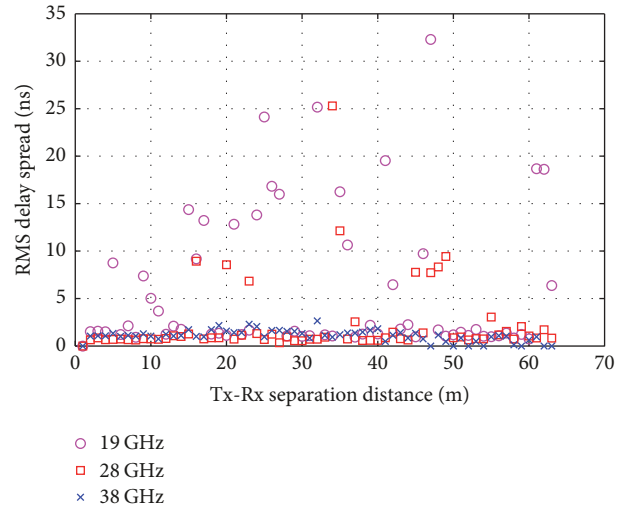

Figure 11: RMS delay spread versus Tx-Rx separation distance at all measured frequencies for the LOS scenario.

Figure 12 shows the CDF for the RMS delay spread in the NLOS scenario for all combined AOAs at all measured bands. A total of 90% of the RMS delay spread is found to be less than 70 ns, 60 ns, and 90 ns for 19, 28, and 38 GHz, respectively. For the NLOS scenario, the delay spread is larger than the LOS scenario because no directed path is received and only the MPCs are captured.

The impact of the angle of arrival (AOA) on the propagation received power is investigated based on the conducted measurements in the NLOS scenario. Here, we set the −120 dBm equipment sensitivity parameter as the noise floor; hence, signals with received powers below this value are considered to be very weak or nonexistent. The received signal powers during the measurement at 0° to 330° AOAs with an interval of 30° in four different spatial locations of 3 m, 4 m, 5 m, and 6 m for the NLOS scenario are shown in Figure 13. The received signal power at four different spatial locations is found to vary with the AOA. In general, the variation occurs more for signals at higher frequency. The results in Figure 13 show that the signals can be received from all measured AOAs at the lower band of 19 GHz for all

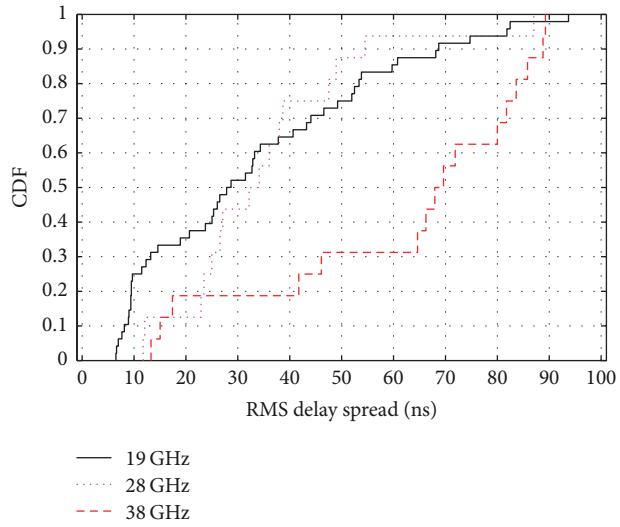

Figure 12: CDF for RMS delay spread at all measured frequencies for the NLOS scenario.

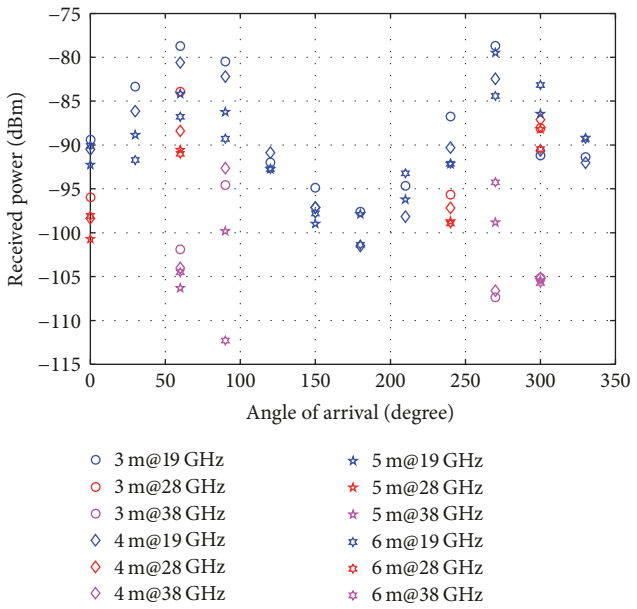

Figure 13: Received power versus AOA for all measured bands at different distances in the NLOS scenario.

4 different spatial locations. This, however, does not occur during measurement at the higher mmWave of 28 GHz and 38 GHz. Another notable observation from Figure 13 is that the variation of received signal power occurs at different AOAs and occurs at different spatial locations. The variation of the received signal power at different spatial locations is found to be greater at high frequency. The result in Figure 13 shows that, at an AOA of 90°, the received signal power decreased more than 10 dB for 1 m changes (from 5 m to 6 m) at 38 GHz, whereas the variation is only approximately 3 dB at 19 GHz within the same separation distance change. Another observation from the results in Figure 13 is that the received signal power is less at the shortest distance than at the largest distance, that is, at an AOA of 270°, the received signal power at 5 m is approximately 4 dB less than that that at 6 m at 38 GHz. It is accordingly clear that this trend is not monotonic with distance, angle, and frequency because of the MPC constructive and destructive phenomena.

Table 2: Angular spread parameters.

Parameter	28 GHz		38 GHz	
	3 m	6 m	3 m	6 m
Λ_{ASA} [degree]	57.9	100.5	13.4	21
μ_{ASA} [degree]	74.8	247.7	90.6	268

Figures 14(a) and 14(b) show the normalized power versus time of arrival (TOA) at different AOAs for the 28 GHz NLOS measurement at 3 m and 6 m distances, respectively. Here, Figure 14 presents the results for only 4 AOAs with the highest received signal power. The figure shows the impact of the signal arriving at different AOAs within the same propagation time delay. The figure also shows that the MPCs are dense for measurement with an NLOS distance of 3 m, whereas they are sparse at 6 m, as shown in Figure 14(b). Interesting observations are made when comparing the MPCs recorded during measurement at AOAs of 0° and 300° for measurement at 3 m. From the NLOS setup in Figure 2, measurement at 0° AOA is perpendicular to the propagation path from the LOS measurement, making it the shortest NLOS path. In Figure 14(a), the NLOS measurement at 28 GHz, however, showed that the signal at 0° AOA measurement has a higher time of arrival value when compared to the signal at 300° AOA. This observation illustrates the severe constructive and deconstructive interference that occurs when using a higher mmWave band for communications. Our results further showed the increased impact of the constructive and destructive interference scenario during higher propagation measurement of the 38 GHz band, as illustrated in Figure 15, where there are no received signals detected during 0° AOA measurement, even though it corresponds to the shortest NLOS path between the transmitter and receiver. The first 38 GHz signal to arrive at the receiver occurs at an AOA of 90° in Figure 15(a) and 300° in Figure 15(b) for a measurement conducted at the NLOS distances of 3 m and 6 m, respectively.

The AOA measurement results for the NLOS scenario in Figures 13, 14, and 15 indicate the significant impact of constructive and destructive interference for propagating signals at mmWave. This phenomenon can be exploited to improve signal reception using a receiver equipped with advanced signal processing and beamforming technology to substantially increase the signal-to-noise ratio (SNR) at the desired user by using the adaptive antenna system and diversity combining.

The angular spread parameters for 28 GHz and 38 GHz are estimated at 3 m and 6 m based on (9) and (10). The angular spread parameters are listed in Table 2. Note that the RMS angular spread and mean angle at 6 m are greater than that those at 3 m for both measured frequencies. This implies that the channel at 6 m can be effectively used to provide rich diversity for a multiple antenna system.

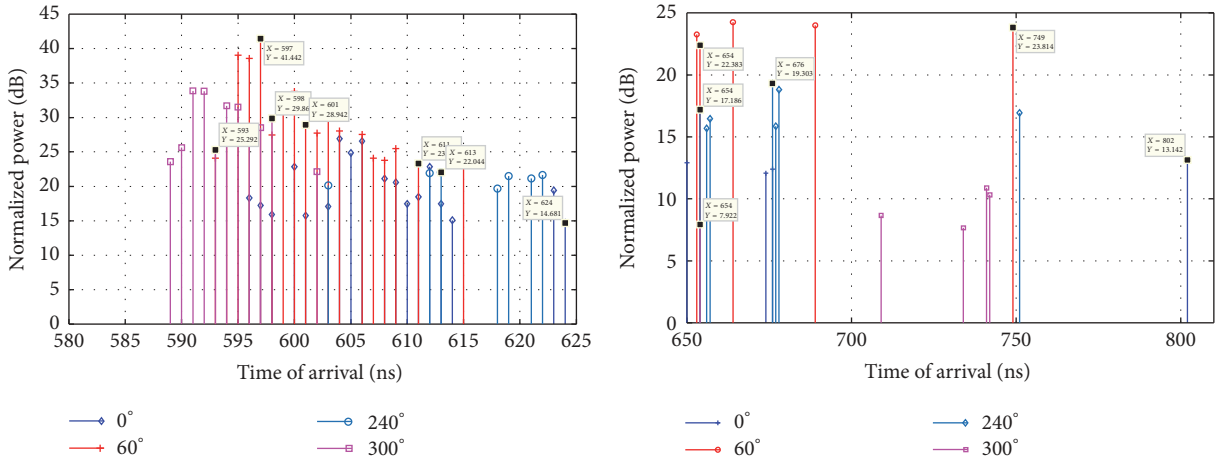

(a) Normalized power versus TOA at 3 m for different AOAs (b) Normalized power versus TOA at 6 m for different AOAs

FIGURE 14: Example of some MPCs in a snapshot of CIR at 28 GHz for the NLOS scenario (a) at 3 m and (b) at 6 m.

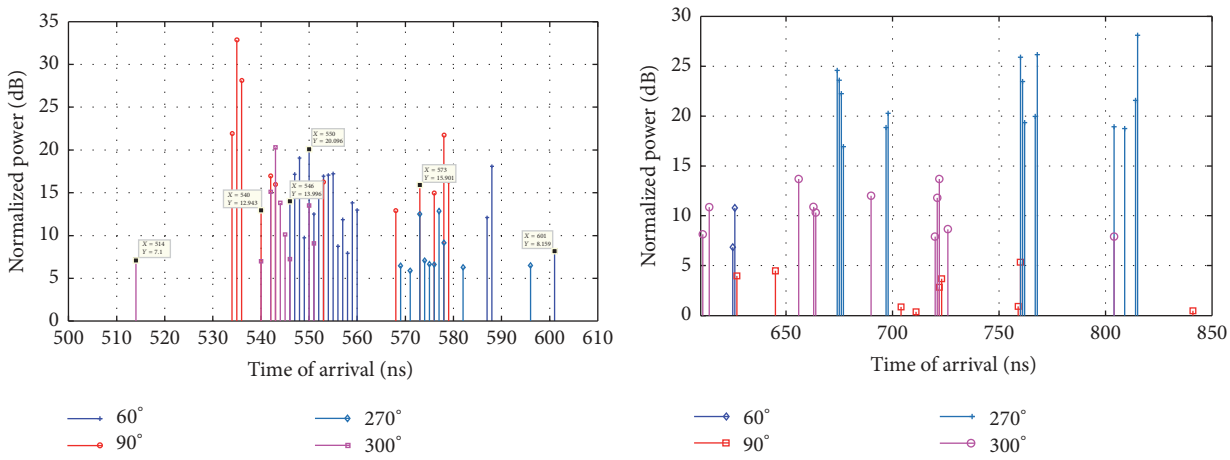

(a) Normalized power versus TOA at 3 m for different AOAs (b) Normalized power versus TOA at 6 m for different AOAs

FIGURE 15: Example of some MPCs in a snapshot of CIR at 38 GHz for the NLOS scenario (a) at 3 m and (b) at 6 m.

7. Conclusion

This paper presented the channel propagation characteristics for three different frequency bands: 19 GHz, 28 GHz, and 38 GHz. The wideband measurements were conducted by using a 5G channel sounder with a high chip rate of 1000 Mcps. The measurement data were processed to obtain the channel impulse response (CIR) via the SAGE algorithm utilizing SystemVue software and MATLAB Toolbox. The path loss, angular spread, and RMS delay spread parameter for the three investigated frequency bands were then computed and analyzed. The CI, FI, FA, ABG, and CIF models were applied to investigate the path loss behavior for the three frequency bands in an indoor LOS environment. The path loss exponents for the LOS scenario were found to vary in the range of 0.6 to 1.3 for all models at the measured frequencies. These values are lower than the free space path loss exponent of 2 because of the wave-guiding effect from both wall sides of the corridor. Our analysis on the time dispersion parameters showed that RMS delay spread values were low for the LOS scenario and that the highest energy arrived with the earliest MPCs. The RMS angular spread varies from 13.4° to 100.5° in the NLOS scenario. Finally, the impact of the angle of arrival (AOA) to the propagation received power was investigated based on the conducted measurement in the NLOS scenario. We found that the received signal power at the higher frequency band is more sensitive to the AOA variation. It is shown that, within a 1-m receiver movement, the received signal power decreases by up to 11 dB when using the 38 GHz band, and the signal only decreased approximately 3 dB for the 19 GHz band. In future work, to estimate the technology gap between 5G and 4G, it is useful to compare the performance of communicating using 28 GHz and 38 GHz with the LTE frequency band, that is, 2.6 GHz.

Conflicts of Interest

The authors declare that there are no conflicts of interest regarding the publication of this paper.

Acknowledgments

The authors would like to thank the Research Management Centre (RMC) at Universiti Teknologi Malaysia for funding this work under Grant no. Q.J130000.21A2.03E69. In addition, the authors would like to acknowledge the Universiti Teknologi Malaysia (UTM) Research Grant (Vot 4J218).

References

[1] F. B. Tesema, A. Awada, I. Viering, M. Simsek, and G. P. Fettweis, "Multiconnectivity for mobility robustness in standalone 5G ultra dense networks with intrafrequency cloud radio access," *Wireless Communications and Mobile Computing*, vol. 2017, Article ID 2038078, 17 pages, 2017.

[2] M. Matalatala, M. Deruyck, E. Tanghe, L. Martens, and W. Joseph, "Performance evaluation of 5G millimeter-wave cellular access networks using a capacity-based network deployment tool," *Mobile Information Systems*, vol. 2017, Article ID 3406074, 11 pages, 2017.

[3] A. Gupta and R. K. Jha, "A survey of 5G network: architecture and emerging technologies," *IEEE Access*, vol. 3, pp. 1206–1232, 2015.

[4] S. Rangan, T. S. Rappaport, and E. Erkip, "Millimeter-wave cellular wireless networks: potentials and challenges," *Proceedings of the IEEE*, vol. 102, no. 3, pp. 366–385, 2014.

[5] T. S. Rappaport, G. R. MacCartney, M. K. Samimi, and S. Sun, "Wideband millimeter-wave propagation measurements and channel models for future wireless communication system design," *IEEE Transactions on Communications*, vol. 63, no. 9, pp. 3029–3056, 2015.

[6] Y. Niu, Y. Li, D. Jin, L. Su, and A. V. Vasilakos, "A survey of millimeter wave communications (mmWave) for 5G: opportunities and challenges," *Wireless Networks*, vol. 21, no. 8, pp. 2657–2676, 2015.

[7] A. F. Elrefaie and M. Shakouri, "Propagation measurements at 28 GHz for coverage evaluation of local multipoint distribution service," in *Proceedings of the Wireless Communications Conference*, pp. 12–17, IEEE, Colorado, Colo, USA, 1997.

[8] H. Xu, T. S. Rappaport, R. J. Boyle, and J. H. Schaffner, "38 GHz wideband point-to-multipoint radio wave propagation study for a campus environment," in *Proceedings of the IEEE 49th Vehicular Technology Conference. Moving Into a New Millenium*, pp. 1575–1579, IEEE, Texas, Tex, USA, 1999.

[9] E. J. Violette, R. H. Espeland, R. O. DeBolt, and F. Schwering, "Millimeter-wave propagation at street level in an urban environment," *IEEE Transactions on Geoscience and Remote Sensing*, vol. 26, no. 3, pp. 368–380, 1988.

[10] F. K. Schwering, E. J. Violette, and R. H. Espeland, "Millimeter-wave propagation in vegetation: experiments and theory," *IEEE Transactions on Geoscience and Remote Sensing*, vol. 26, no. 3, pp. 355–367, 1988.

[11] A. M. Al-Samman, T. A. Rahman, M. H. Azmi et al., "Statistical modelling and characterization of experimental mm-wave indoor channels for future 5G wireless communication networks," *PLoS ONE*, vol. 11, no. 9, pp. 1–29, 2016.

[12] X. Wu, Y. Zhang, C. Wang, G. Goussetis, M. Aggoune, and M. M. Alwakeel, "28 GHz indoor channel measurements and modelling in laboratory environment using directional antennas," in *Proceedings of the 2015 9th European Conference, Antennas Propag (EuCAP)*, pp. 1–5, 2015.

[13] S. Sun, T. S. Rappaport, T. A. Thomas et al., "Investigation of prediction accuracy, sensitivity, and parameter stability of large-scale propagation path loss models for 5G wireless communications," *IEEE Transactions on Vehicular Technology*, vol. 65, no. 5, pp. 2843–2860, 2016.

[14] G. R. Maccartney, M. K. Samimi, and T. S. Rappaport, "Omnidirectional path loss models in New York City at 28 GHz and 73 GHz," in *Proceedings of the 2014 25th IEEE Annual International Symposium on Personal, Indoor, and Mobile Radio Communication, IEEE PIMRC 2014*, pp. 227–231, IEEE, Washington, Wash, USA, September 2014.

[15] S. Deng, M. K. Samimi, and T. S. Rappaport, "28 GHz and 73 GHz millimeter-wave indoor propagation measurements and path loss models," in *Proceedings of the IEEE International Conference on Communication Workshop, ICCW '15*, pp. 1244–1250, London, UK, June 2015.

[16] G. R. MacCartney, S. Deng, and T. S. Rappaport, "Indoor office plan environment and layout-based mmWave path loss models for 28 GHz and 73 GHz," in *Proceedings of the 2016 IEEE 83rd Vehicular Technology Conference (VTC Spring)*, pp. 1–6, IEEE, Nanjing, China, May 2016.

[17] S. Nie, G. R. MacCartney, S. Sun, and T. S. Rappaport, "72 GHz millimeter wave indoor measurements for wireless and backhaul communications," in *Proceedings of the IEEE 24th Annual International Symposium on Personal, Indoor, and Mobile Radio Communications (PIMRC '13)*, pp. 2429–2433, IEEE, London, UK, September 2013.

[18] N. Zhang, X. Yin, S. X. Lu, M. Du, and X. Cai, "Measurement-based angular characterization for 72 GHz propagation channels in indoor environments," in *Proceedings of the 2014 IEEE Globecom Workshops, GC Wkshps 2014*, pp. 370–376, Texas, Tex, USA, December 2014.

[19] S. Geng and P. Vainikainen, "Millimeter-wave propagation in indoor corridors," *IEEE Antennas and Wireless Propagation Letters*, vol. 8, pp. 1242–1245, 2009.

[20] M. Kyrö, K. Haneda, J. Simola et al., "Measurement based path loss and delay spread modeling in hospital environments at 60 GHz," *IEEE Transactions on Wireless Communications*, vol. 10, no. 8, pp. 2423–2427, 2011.

[21] W. Roh, J.-Y. Seol, J. Park et al., "Millimeter-wave beamforming as an enabling technology for 5G cellular communications: theoretical feasibility and prototype results," *IEEE Communications Magazine*, vol. 52, no. 2, pp. 106–113, 2014.

[22] K. Haneda, L. Tan, Y. Zheng et al., "5G 3GPP-like channel models for outdoor urban microcellular and macrocellular environments," in *Proceedings of the 2016 IEEE 83rd Vehicular Technology Conference (VTC Spring)*, pp. 1–7, IEEE, Nanjing, China, May 2016.

[23] S. Hur, Y.-J. Cho, J. Lee, N.-G. Kang, J. Park, and H. Benn, "Synchronous channel sounder using horn antenna and indoor measurements on 28 GHz," in *Proceedings of the IEEE International Black Sea Conference on Communications and Networking (BlackSeaCom '14)*, pp. 83–87, IEEE, Odessa, Ukraine, May 2014.

[24] M. Lei, J. Zhang, T. Lei, and D. Du, "28 GHz indoor channel measurements and analysis of propagation characteristics," in *Proceedings of the 2014 25th IEEE Annual International Symposium on Personal, Indoor, and Mobile Radio Communication,*

IEEE PIMRC '14, pp. 208–212, IEEE, Washington, Wash, USA, September 2014.

[25] Q. Wang, S. Li, X. Zhao, M. Wang, and S. Sun, "Wideband millimeter-wave channel characterization based on los measurements in an open office at 26 GHz," in *Proceedings of the 2016 IEEE 83rd Vehicular Technology Conference (VTC Spring)*, pp. 1–5, IEEE, Nanjing, China, May 2016.

[26] S. Brochure, "Keysight Technologies 5G Channel Sounding," http://about.keysight.com/en/newsroom/pr/2015/30jul-em15109.shtml.

[27] "SystemVue Software, 2217697, 2015," http://www.keysight.com/main/software.jspx?cc=MY&lc=eng&ckey=2217697&nid=-34264.804607.02&id=2217697&cmpid=zzfindeesof-Systemvue-Latest-Downloads.

[28] M. Kyrö, V.-M. Kolmonen, and P. Vainikainen, "Experimental propagation channel characterization of mm-wave radio links in urban scenarios," *IEEE Antennas and Wireless Propagation Letters*, vol. 11, pp. 865–868, 2012.

[29] X. Yin, Y. He, Z. Song, M.-D. Kim, and H. K. Chung, "A sliding-correlator-based SAGE algorithm for Mm-wave wideband channel parameter estimation," in *Proceedings of the 8th European Conference on Antennas and Propagation, EuCAP '14*, pp. 625–629, IEEE, The Hague, Netherlands, April 2014.

[30] J. A. Fessler and A. O. Hero, "Space-alternating generalized expectation-maximization algorithm," *IEEE Transactions on Signal Processing*, vol. 42, no. 10, pp. 2664–2677, 1994.

[31] A. M. Al-Samman, M. H. Azmi, T. A. Rahman, I. Khan, M. N. Hindia, and A. Fattouh, "Window-based channel impulse response prediction for time-varying ultra-wideband channels," *PLoS ONE*, vol. 11, no. 12, Article ID e0164944, 2016.

[32] A. Muqaibel, A. Safaai-Jazi, S. Riad, A. Attiya, and B. Woerner, "Path-loss and time dispersion parameters for indoor UWB propagation," *IEEE Transactions on Wireless Communications*, vol. 5, no. 3, pp. 550–559, 2006.

[33] C. W. Kim, X. Sun, L. C. Chiam, B. Kannan, F. P. S. Chin, and H. K. Garg, "Characterization of ultra-wideband channels for outdoor office environment," in *Proceedings of the 2005 IEEE Wireless Communications and Networking Conference, WCNC '05: Broadband Wirelss for the Masses - Ready for Take-off*, pp. 950–955, IEEE, Louisiana, La, USA, March 2005.

[34] A. F. Molisch and F. Tufvesson, "Propagation channel models for next-generation wireless communications systems," *IEICE Transactions on Communications*, vol. E97.B, no. 10, pp. 2022–2034, 2014.

[35] A. M. Al-Samman, T. A. Rahman, M. Hadri, I. Khan, and T. H. Chua, "Experimental UWB indoor channel characterization in stationary and mobility scheme," *Measurement*, vol. 111, pp. 333–339, 2017.

[36] A. M. Al-Samman and T. A. Rahman, "Experimental characterization of multipath channels for ultra-wideband systems in indoor environment based on time dispersion parameters," *Wireless Personal Communications*, vol. 95, no. 2, pp. 1713–1724, 2017.

[37] T. Jiang, L. Tian, P. Tang, Z. Hu, and J. Zhang, "Basestation 3-dimensional spatial propagation characteristics in urban microcell at 28 GHz," in *Proceedings of the 11th European Conference on Antennas and Propagation, EUCAP '17*, pp. 3167–3171, IEEE, Paris, France, March 2017.

[38] G. R. MacCartney, T. S. Rappaport, S. Sun, and S. Deng, "Indoor office wideband millimeter-wave propagation measurements and channel models at 28 and 73 GHz for ultra-dense 5G wireless networks," *IEEE Access*, vol. 3, pp. 2388–2424, 2015.

[39] T. S. Rappaport, *Wireless Communications Principles and Practice*, 2nd edition, 2002.